ACCEPTED MANUSCRIPT · OPEN ACCESS

NNETFIX: An artificial neural network-based denoising engine for gravitational-wave signals

To cite this article before publication: Kentaro Mogushi et al 2021 Mach. Learn.: Sci. Technol. in press https://doi.org/10.1088/2632-2153/abea69

Manuscript version: Accepted Manuscript

Accepted Manuscript is "the version of the article accepted for publication including all changes made as a result of the peer review process, and which may also include the addition to the article by IOP Publishing of a header, an article ID, a cover sheet and/or an 'Accepted Manuscript' watermark, but excluding any other editing, typesetting or other changes made by IOP Publishing and/or its licensors"

This Accepted Manuscript is © 2021 The Author(s). Published by IOP Publishing Ltd.

As the Version of Record of this article is going to be / has been published on a gold open access basis under a CC BY 3.0 licence, this Accepted Manuscript is available for reuse under a CC BY 3.0 licence immediately.

Everyone is permitted to use all or part of the original content in this article, provided that they adhere to all the terms of the licence https://creativecommons.org/licences/by/3.0

Although reasonable endeavours have been taken to obtain all necessary permissions from third parties to include their copyrighted content within this article, their full citation and copyright line may not be present in this Accepted Manuscript version. Before using any content from this article, please refer to the Version of Record on IOPscience once published for full citation and copyright details, as permissions may be required. All third party content is fully copyright protected and is not published on a gold open access basis under a CC BY licence, unless that is specifically stated in the figure caption in the Version of Record.

View the article online for updates and enhancements.

NNETFIX: An artificial neural network-based denoising engine for gravitational-wave signals

Kentaro Mogushi

Institute of Multi-messenger Astrophysics and Cosmology, Missouri University of Science and Technology, Physics Building, 1315 N. Pine St., Rolla, MO 65409, USA

Ryan Quitzow-James

Institute of Multi-messenger Astrophysics and Cosmology, Missouri University of Science and Technology, Physics Building, 1315 N. Pine St., Rolla, MO 65409, USA

Marco Cavaglià

Institute of Multi-messenger Astrophysics and Cosmology, Missouri University of Science and Technology, Physics Building, 1315 N. Pine St., Rolla, MO 65409, USA

Sumeet Kulkarni

Department of Physics and Astronomy, University of Mississippi, MS 38677-1848, USA

Fergus Hayes

SUPA, School of Physics and Astronomy, University of Glasgow, Glasgow G12 8QQ, United Kingdom

2 February 2021

Abstract. Instrumental and environmental transient noise bursts in gravitational-wave detectors, or glitches, may impair astrophysical observations by adversely affecting the sky localization and the parameter estimation of gravitational-wave signals. Denoising of detector data is especially relevant during low-latency operations because electromagnetic follow-up of candidate detections requires accurate,

rapid sky localization and inference of astrophysical sources. NNETFIX is a machine learning, artificial neural network-based algorithm designed to estimate the data containing a transient gravitational-wave signal with an overlapping glitch as though the glitch was absent. The sky localization calculated from the denoised data may be significantly more accurate than the sky localization obtained from the original data or by removing the portion of the data impacted by the glitch. We test NNETFIX in simulated scenarios of binary black hole coalescence signals and discuss the potential for its use in future low-latency LIGO-Virgo-KAGRA searches. In the majority of cases for signals with a high signal-to-noise ratio, we find that the overlap of the sky maps obtained with the denoised data and the original data is better than the overlap of the sky maps obtained with the original data and the data with the glitch removed.



1. Introduction

The field of gravitational-wave (GW) astronomy began with the first direct detection of a GW signal from a binary black hole (BBH) merger [1] on September 14th, 2015. Nine additional BBH mergers were detected with high confidence during the first and second LIGO [2] and Virgo [3] observation runs (O1 and O2) [4]. During the first half of the third LIGO-Virgo observation run (O3a), 39 binary merger events were detected with high confidence [5], including two exceptional BBH events [6–8] and a possible neutron star and black hole (NSBH) merger [9].

On August 17th, 2017, the first detection of a GW signal from a binary neutron star (BNS) merger, GW170817, expanded multi-messenger astronomy to include GW observations [10]. A short gamma-ray burst (GRB) was detected approximately 1.7 seconds after the BNS merger time [11]. The sky map calculated from the GW signal allowed the identification of the event with an electromagnetic (EM) counterpart [10, 11]. The association of this GW event with the observed EM transients supports the long-hypothesized model that at least some short GRBs are due to BNS coalescences [12] and has provided many insights into fundamental astrophysics and cosmology. In April 2020, a second BNS merger without an EM counterpart was detected [13].

In order to detect GW signals, ground-based GW detectors must be extremely sensitive, causing them to become highly susceptible to instrumental and environmental noise [4]. In particular, transient noise bursts, or *glitches*, may impair the quality of detector data. The presence of a glitch in the proximity of a GW signal can adversely affect the analysis of the latter, including calculating the sky localization of the source. The most notable example of such an occurrence was GW170817, where the effect of a glitch was mitigated in low-latency by removing the contaminated portion of the data and in follow-up studies by applying ad hoc mitigation algorithms [10,14].

Eleven confident detections out of the 50 observed in O1, O2 and O3a required some form of ad hoc analysis to mitigate the effect of glitches on the estimation of candidate event parameters [4, 5]. Given a single-detector glitch rate of 0.007 Hz with signal-to-noise ratio (SNR) larger than 7.5 [15] and a percentage of observing time with two detectors operating in coincidence of $\sim 80\%$ in O3a [5], the probability of a glitch overlapping a signal in one detector is over 1% for a signal duration of a few seconds (typical of a BBH event) and may be up to $\sim 30\%$ for a BNS event

with a typical duration of a minute or more. Given the expected detection rate of astrophysical signals in the planned fourth LIGO-Virgo-KAGRA run (O4) and later runs, and the increased sensitivity in the detectors likely leading to an increased glitch rate, we expect a significant number of detections to overlap with glitches.

One possibility to mitigate the effect of a contaminating glitch would be to discard the data from the affected detector. This is the simplest and fastest solution; however, it is also likely to impact the analysis and sky localization, especially in cases where data is only available from two detectors. Another technique that can be used in low-latency is *gating*, which removes the data affected by the glitch. One method of gating is to set the data affected by the glitch to zero using a window function to smoothly transition into and out of the gate [16]. Gating was used in the case of GW170817 to produce the low-latency sky localization for EM follow-up observations [17]. On larger latencies, glitch mitigation techniques such as using BayesWave [18] to model and subtract the glitch can be used [17, 19, 20].

Figure 1 shows an example of the detrimental effect gating data can have on the sky localization error region of a simulated BBH merger signal. The sky localization obtained with the gated data significantly differs from the sky localization estimated from the full data. Also, the 90% sky localization error region after the gating is applied no longer includes the true sky position of the injected signal.

The higher detector sensitivity of LIGO and Virgo in their third observing run has led to an increased number of GW candidate detections from different astrophysical populations [6,9,13]. Future observation runs with higher sensitivity are expected to produce even greater detection rates, which would lead to higher chances of observing GW signals contaminated by glitches. The inability to accurately estimate the sky localization of GW candidates with potential EM counterparts due to glitches contaminating the signal could put at risk new astrophysical discoveries such as those made with GW170817. Thus, the development and implementation of accurate low-latency denoising methods could be highly beneficial to multi-messenger observations.

In recent years, machine learning algorithms have been in development to classify detector noise and reduce its effect on GW signals [21]. In particular, there have been many efforts in applying different techniques involving neural networks. GravitySpy uses citizen science to provide a data set used to train convolutional neural network (CNN) based deep learning image classifiers to identify and classify noise transients [15]. Other efforts include development of an algorithm based on

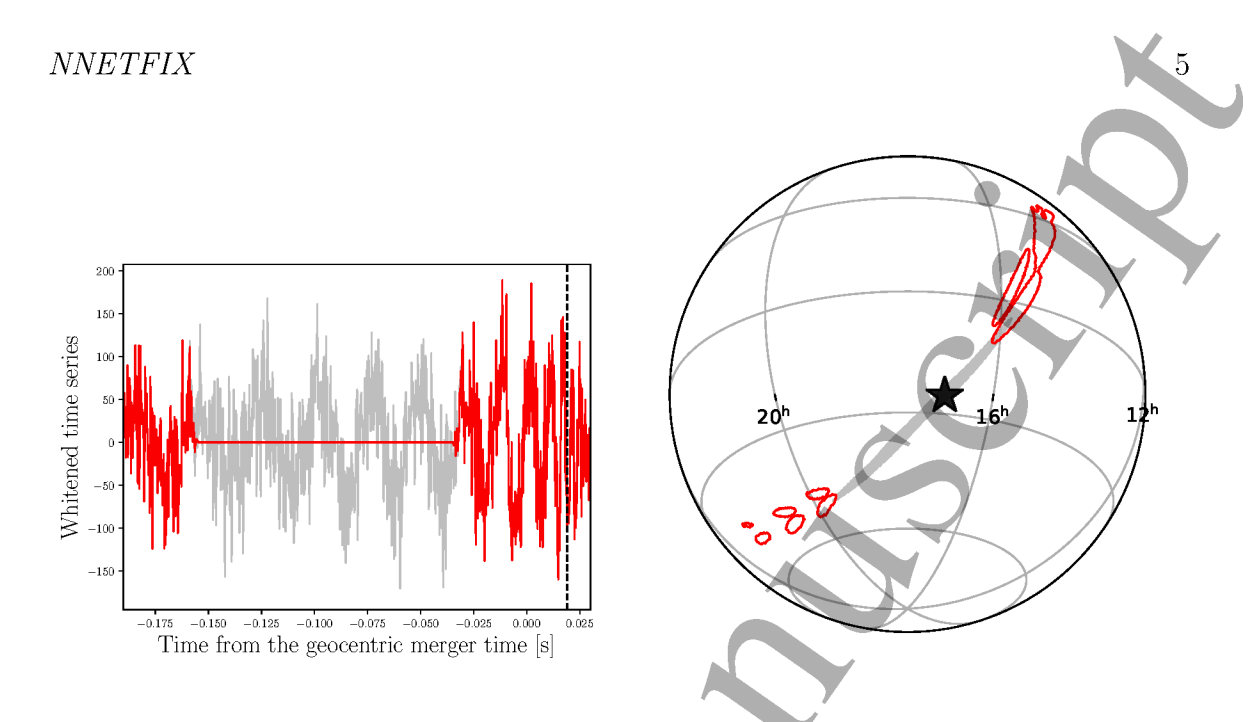


Figure 1. Left: Whitened time series of a simulated BBH signal with two-detector network SNR $\rho_{\rm N}=42.4$ and component masses $(m_1,m_2)=(35,29)~M_{\odot}$ in advanced LIGO (aLIGO) recolored Gaussian noise (red curve). A 130 ms gate is applied 30 ms before the geocentric merger time (gray curve). The vertical black-dashed line denotes the merger time in LIGO-Hanford (H1). Right: The 90% sky localization error regions from the full data (gray area) and the gated data (red empty contours). The star indicates the true sky position of the simulated signal.

a total variational method for noise reduction assisted by the use of an artificial neural network (ANN) [22], DeepClean, a long short-term memory neural network that has many layers and uses witness channels for noise subtraction [23], and work done to denoise GW data using CNNs [24]. There has also been research into using ANNs to quickly calculate the sky localization of candidate signals using the raw and processed strain data from GW detectors [25]. A thorough overview of this subject is presented in Ref. [21].

In this paper, we present a machine learning-based algorithm to denoise transient GW signals called NNETFIX ("A Neural NETwork to 'FIX' GW signals coincident with short-duration glitches in detector data"). The output from NNETFIX can be used as input to other algorithms such as BAYESTAR [26] to produce sky maps or LALInference [27] or Bilby [28] to perform parameter estimation. NNETFIX uses ANNs to estimate the portion of a signal which is lost due to the presence of an

NNETFIX 6

overlapping glitch. We train the ANN to reconstruct the portion of a gated signal on a template bank of BBH waveforms injected into simulated noise data. The accuracy of the algorithm is assessed by comparing the recovered waveform, SNR, and sky map from the processed data to the corresponding quantities obtained before gating. We derive a set of statistical metrics to assess the improvement in these quantities.

2. Algorithm implementation, training and testing

We consider a scenario in which a transient BBH GW signal is observed by a network of at least two detectors and the data of one detector is partially gated to remove an overlapping glitch identified by software such as Omicron [29] or iDQ [30, 31]. Without loss of generality, we perform the analysis for the two LIGO detectors, LIGO-Hanford (H1) and LIGO-Livingston (L1), with the gating applied to data from the H1 detector. We assume the merger time at the geometric center of Earth (or geocentric merger time) to be (approximately) known from L1 data. We denote with $s_f(t)$, $s_g(t)$ and $s_r(t)$ the full time series without the glitch, the gated time series, and the NNETFIX reconstructed time series, respectively. The output of NNETFIX can be thought of as the map

$$s_r(t) := F[s_g(t)] . (1)$$

We train an ANN regression algorithm to construct the map F such that $s_r(t) \sim s_f(t)$. The NNETFIX implementation uses the SCIKIT-LEARN [32] Multi-Layered Perceptron (MLP) Regressor, a type of ANN in which the artifical neurons (mathematical functions) are arranged into layers and connected to every neuron in the preceding and/or succeeding layers [33]. Each neuron calculates a weighted linear combination of the outputs from the preceding layer and applies an activation function that introduces a non-linearity into the neuron's output. The ANN trained by NNETFIX consists of one hidden layer containing 200 neurons. This configuration is similar to the one employed in Ref. [22] based on a single hidden layer with 40 neurons. Multi-layer configurations have been used by other denoising algorithms, such as DeepClean [23] and the CNN-based algorithm in Ref. [24]. In the ANN training process, NNETFIX uses the rectified linear unit (ReLU) activation function [34,35] and the ADAM stochastic gradient-based optimizer [36] with a learning rate of 10^{-3} . Ten percent of the training data samples are set aside and used for validating the training. The training iteration stops if the ANN performance plateaus with a

tolerance level of 10^{-4} to avoid overtraining. To reconstruct the gated portion of the time series, one hidden layer works better than multiple hidden layers for the loss function of mean square error and the number of hidden layers tested. The values from the loss function have a weak dependency on the number of neurons.

To train the algorithm, we first build template banks of simulated non-spinning IMRPHENOMD BBH merger waveforms [37] with varying intrinsic and extrinsic parameters. To reduce the potential for overtraining, each template bank also includes a number of (pure) noise time series. We distribute the positions of the injected signals isotropically in the sky. The waveform coalescence phase, polarization angle, and cosine of the inclination angle are uniformly distributed in the intervals $[0, 2\pi]$, $[0, \pi]$, and [-1, 1], respectively. We uniformly distribute the network SNR ρ_N [16] of the simulated signals in the range [11.3, 42.4]. We consider three distinct template banks corresponding to low, medium, and high BBH component masses to assess the prediction accuracy of the trained ANNs for different signal lengths. The BBH component masses are uniformly sampled according to a Jeffreys prior for the matched-filter detection statistic. As the mass of the system decreases, we employ a higher number of templates to properly cover the mass parameter space [38–41].

For each of the three distinct template banks, we build 12 training+testing (TT) sets: first, we inject each waveform into 50 distinct realizations of recolored Gaussian noise for advanced LIGO (aLIGO) at design sensitivity; second, we include the (pure) noise time series; third, we shuffle and split the set by 70%–30% for training and testing, with 10% of the training set used for internal validation; and finally, we apply the 12 combinations of gate durations $t_d = (50, 75, 130)$ ms and gate end-times before the geocentric merger time $t_e = (15, 30, 90, 170)$ ms. The time series are sampled at 4096 Hz, whitened, and high-passed. A conservative value of 25 Hz is used for the high-pass filter. The gates are implemented as a reversed Tukey window with a taper of 0.1 s and held fixed with respect to geocentric merger time; however, the merger time seen in the H1 detector naturally shifts due to the sky position and the polarization angle of the GW signal. Table 1 shows the range of the component masses, the number of waveforms, the number of noise series, and the dimension of the sets for the different scenarios.

We test the effectiveness of the ANNs by calculating the coefficient of determination for the MLP Regressor in SCIKIT-LEARN on the testing sets [32]. The coefficient of determination ranges from $-\infty$ (bad) to 1 (perfect estimation), with

| | $m_1 \ [M_{\odot}]$ | $m_2~[M_{\odot}]$ | n_s | n_n | Set dimension $(n_s \times 50 + n_n)$ |
|-----------------------|---------------------|-------------------|-------|-------|---------------------------------------|
| Low | 10–15 | 8–12 | 348 | 1900 | 19300 |
| Medium | 15 - 25 | 12 - 18 | 251 | 1350 | 13900 |
| High | 28 – 42 | 23 - 35 | 61 | 300 | 3350 |

NNETFIX 8

Table 1. Component mass ranges, number of waveforms (n_s) , number of pure noise series (n_n) , and dimension of the TT sets for each of the three scenarios and combinations of gate durations and end-times.

positive values corresponding to some degree of accuracy. We evaluate the coefficient of determination on each testing set after training the ANN on the corresponding training set. The ranges of the coefficient of determination for the testing sets are [0.773, 0.882], [0.750, 0.883], and [0.691, 0.879] for the low-mass, medium-mass, and high-mass scenarios, respectively, and the means are 0.833, 0.827, and 0.814.

We test for potential statistical effects in the training method by considering the medium-mass scenario with a gate duration of 50 ms and a gate end-time of 30 ms as a representative case. For 100 trials, we find that the coefficient of determination ranges from 0.800 to 0.826 with a mean of 0.815, which is consistent with the ranges of the testing sets.

The effect of NNETFIX on quantities such as SNR and sky localization varies for different component masses, network SNR, and gate settings. Therefore, we construct 108 additional independent exploration sets with fixed network SNR $\rho_{\rm N}=(11.3,\ 28.3,\ 42.4)$ and component masses of $(12,\ 10),\ (20,\ 15),\ (35,\ 29)\ M_{\odot},$ and identical combinations of gate durations and end-times as the TT sets. Each exploration set consists of 512 independent time series with the remaining parameters distributed as in the TT sets.

3. Performance in the time-domain

NNETFIX's performance in estimating the full time series can be assessed by computing the amount of SNR lost in the reconstruction process. We define the fractional residual SNR (FRS)

$$FRS = \frac{\rho_f - \rho_r}{\rho_f} \,, \tag{2}$$

where ρ_f and ρ_r are the (single interferometer) peak SNR of the full time series and the reconstructed time series in H1, respectively. Positive values of FRS close to zero generally indicate accurate time series reconstructions. However, FRS ~ 0 may also occur when the gating does not significantly reduce the peak SNR of the full series, and thus, $\rho_f \sim \rho_g \sim \rho_r$. These cases can be separated by the fractional SNR gain (FSG)

$$FSG = \frac{\rho_r - \rho_g}{\rho_g}, \tag{3}$$

where ρ_g is the peak SNR of the gated series. FSG characterizes the amount of SNR gained by the reconstructed time series in comparison to the gated time series. Typically, NNETFIX performance is better for smaller values of FRS and larger values of FSG.

Median values of FRS across the exploration sets range from FRS = -0.09 (high-mass case with $\rho_N = 11.3$, $t_d = 170$ ms and $t_e = 50$ ms) to FRS = 0.22 (medium-mass case with $\rho_N = 28.3$, $t_d = 15$ ms and $t_e = 130$ ms). Sets with smaller gate durations are generally characterized by lower FRS values. All exploration sets with $t_d = 50$ ms have FRS < 0.1. The fraction of sets with FRS below this threshold reduces to 0.78 and 0.55 for gate durations of 75 ms and 130 ms, respectively. Similarly, exploration sets with gates that are farther away from the time of the merger also tend to have a lower median value of FRS. All sets with gate end-times at 170 ms before merger have median FRS < 0.07 while only 81%, 55% and 11% of the samples with $t_e = 90$, 30 and 15 ms have FRS below this threshold, respectively. The effects of the network SNR and component masses on FRS are less significant. About 83% of the sets with $\rho_N = 11.3$ have median FRS < 0.1 compared to 75% for the sets with $\rho_N = 28.3$ and $\rho_N = 42.4$. The percentages of low-mass, medium-mass and high-mass sets with FRS < 0.1 are comparable at about 78%, 75% and 81%, respectively.

Median values of FSG range from ~ 0.02 (low-mass, low-SNR case with $t_d=170$ ms and $t_e=50$ ms) to ~ 0.89 (high-mass, low-SNR case with $t_d=130$ ms and $t_e=15$ ms). High-mass (low-mass) exploration sets are typically characterized by higher (lower) values of FSG. All high-mass sets have FSG > 0.08, while all low-mass sets have FSG < 0.07. The network SNR does not seem to significantly affect the value of FSG. Gate end-times closer to the merger time tend to result in higher FSG. The value of FSG at $t_e=30$ ms is higher than the value at $t_e=170$ ms by a factor of ~ 2 on average for fixed component masses, network SNR, and gate duration. In contrast, longer gate durations tend to result in higher FSG. The value of FSG at

 $t_d=130$ ms is higher than the value at $t_d=50$ ms by a factor of ~ 2 on average for fixed component masses, network SNR, and gate end-time. Two thirds of the sets with $t_d=130$ ms have FSG > 0.08 compared to only 42% of the sets with $t_d=50$ ms.

We find that a combined threshold of FRS > 0 and FSG > 0.01 selects approximately 70% of the samples across all the exploration sets; 95% of these are successfully reconstructed as defined in the rest of this section. Figure 2 shows the NNETFIX data reconstruction for the time series of Fig. 1. As shown in Fig. 3, the reconstructed time series recovers a large signal energy in the gated portion. In this case, FRS = 0.05 and FSG = 0.53.

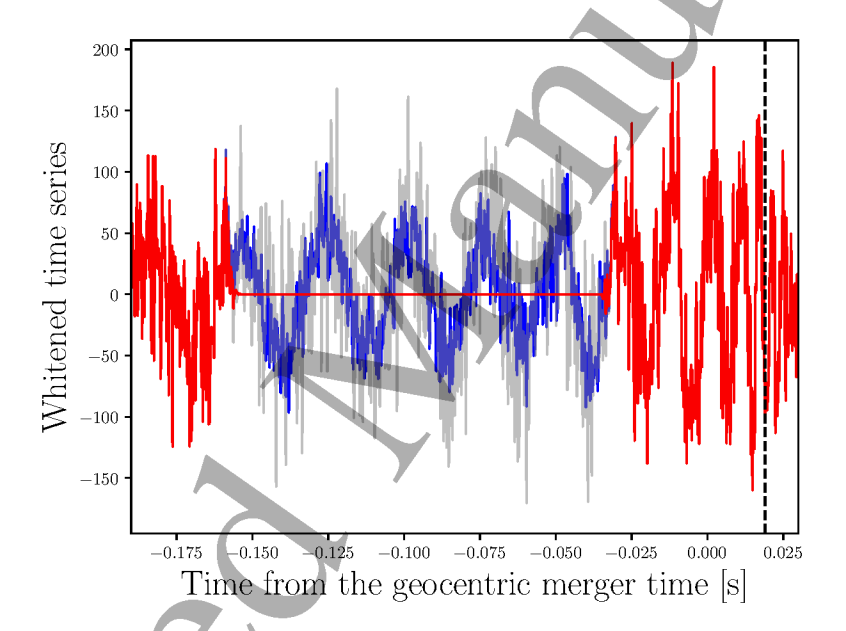


Figure 2. The whitened full time series (gray), the gated time series (red) and the reconstructed time series (blue) for the simulated event of Fig. 1. The vertical black-dashed line denotes the merger time in H1.

A complementary metric to evaluate the performance of the algorithm is the fractional match gain (FMG)

$$FMG = \frac{M_r - M_g}{M_f - M_g}, (4)$$

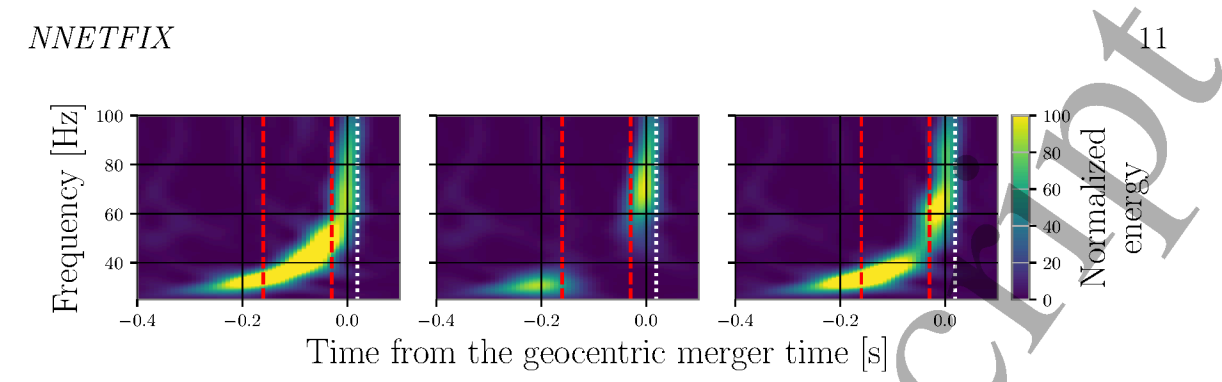


Figure 3. Time frequency representations of the full (left), gated (middle), and reconstructed (right) time series for the simulated event of Fig. 2 using the Q transform [42]. The vertical red-dashed line denotes the gate and the vertical white-dotted line denotes the merger time in H1.

where the match M_i between a time series s_i and the injected waveform h is [43]

$$M_i = \frac{\langle s_i | h \rangle}{\sqrt{\langle s_i | s_i \rangle \langle h | h \rangle}} \,. \tag{5}$$

The inner product of two time series s_i and s_j is defined as

$$\langle s_i | s_j \rangle = 4\Re \int_{f_1}^{f_N} \frac{\tilde{s}_i(f)\tilde{s}_j^*(f)}{S(f)} df ,$$
 (6)

where the tilde indicates the Fourier transform, the star denotes the complex conjugate, S(f) is the detector noise power spectral density (PSD), f_1 is the high-pass frequency, and f_N is the Nyquist frequency.

In Eq. (4), we assume $M_f - M_g > 0$. In rare instances (0.5% of all exploration set data samples), M_g becomes larger than M_f . This occurs for small values of the single interferometer peak SNR (median value of 4.6) when the gated portion of the data is dominated by noise and anti-correlates with the injected waveform. In the following, we remove these data samples from the exploration sets.

FMG assesses how well the NNETFIX reconstructed data matches the signal in comparison to the full data and gated data. Positive (negative) values of FMG correspond to M_r greater (smaller) than M_g , indicating that the NNETFIX reconstructed time series has a better (worse) match with the injected waveform than the gated time series. Values of FMG larger than 1 indicate that the ANN overfits the data, i.e., the reconstructed time series is more similar to the injected

waveform than the full time series. Therefore, we consider the reconstructions with $0 < \mathrm{FMG} \le 1$ to be successful. As noted earlier, 95% of the samples which pass the combined threshold of FRS > 0 and FSG > 0.01 satisfy this condition. Figures 4 and 5 show the distributions of FMG for two exploration sets from the medium-mass scenario. Figure 6 displays the comparison of these distributions.

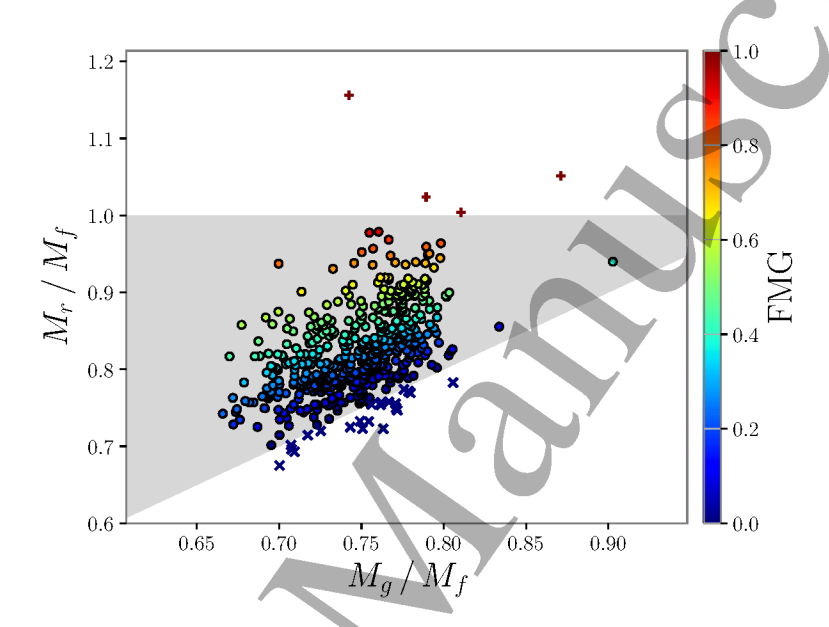


Figure 4. Scatterplot of M_r/M_f vs. M_g/M_f for the exploration set with $\rho_N=42.4$, $(m_1,m_2)=(20,15)~M_{\odot}$, $t_d=130~{\rm ms}$ and $t_e=30~{\rm ms}$. The circles denote samples with $0<{\rm FMG}\le 1$, the \times markers denote samples with FMG ≤ 0 and the + markers denote overfitted samples with FMG > 1. The gray area denotes the region of the parameter space with $0<{\rm FMG}\le 1$, which contains 95% of the reconstructed time series. Two outliers with values FMG=-0.4 and FMG=-0.4 are not shown in the plot in order to improve readability.

We quantify NNETFIX's performance by estimating the reconstruction efficiency, which we define as the fraction of successfully reconstructed samples, i.e., samples with $0 < \text{FMG} \le 1$. The fractions of samples with $\text{FMG} \le 0$, $0 < \text{FMG} \le 1$ and FMG > 1 for all exploration sets are given in Tables 2-4. The efficiency across all exploration sets varies from approximately 0.31 to over 0.95. There is a mild dependence on the component masses of the system; the median value of the efficiency decreases from 0.77 for the low-mass scenario to 0.61 for the high-mass scenario when

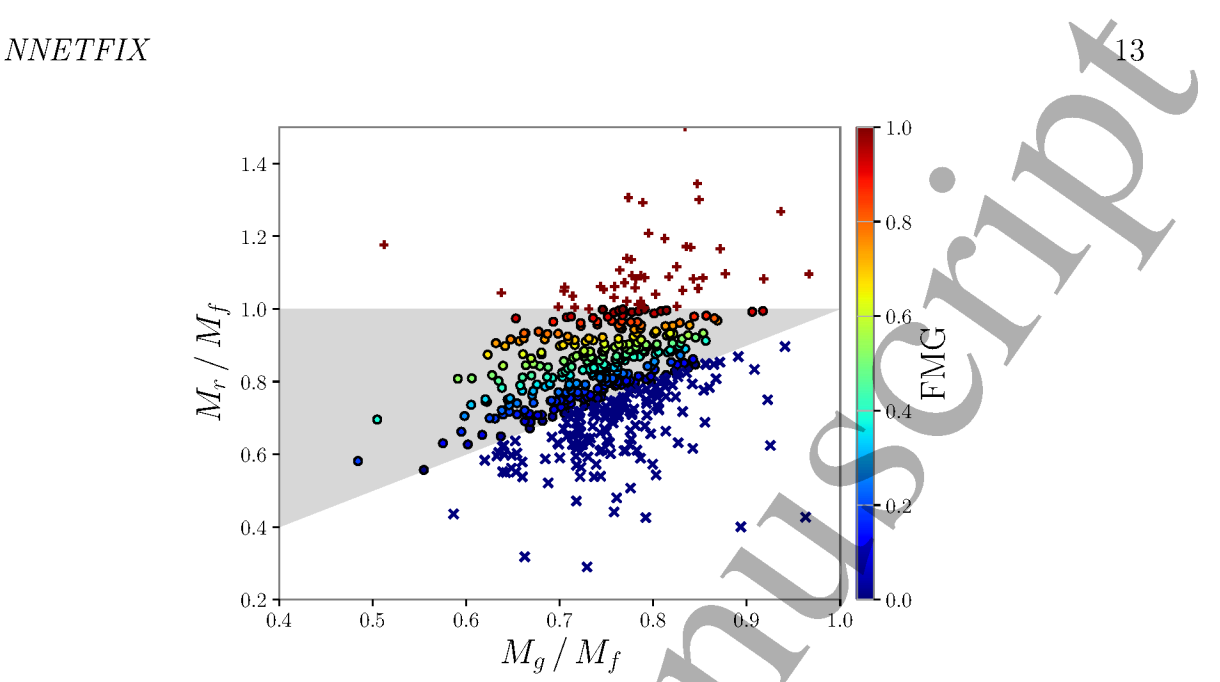


Figure 5. Scatterplot of M_r/M_f vs. M_g/M_f for the exploration set with $\rho_N = 11.3$, $(m_1, m_2) = (20, 15)~M_{\odot}$, $t_d = 130~{\rm ms}$ and $t_e = 30~{\rm ms}$. The circles denote samples with $0 < {\rm FMG} < 1$, the \times markers denote samples with FMG ≤ 0 and the + markers denote overfitted samples with FMG > 1. The gray area denotes the region of the parameter space with $0 < {\rm FMG} \leq 1$, which contains 59% of the reconstructed time series.

all other parameters (network SNR, gate duration and gate end-time) are held fixed. The worst case is the medium-mass scenario with $\rho_N = 11.3$, $t_e = 170$ ms, and $t_d = 130$ ms, in which 68% of the samples are unsuccessfully reconstructed.

Within each mass scenario when the gate duration and gate end-time are held fixed, NNETFIX's efficiency typically improves by a factor $\sim 1.5-2$ as the network SNR increases. As the SNR becomes higher, the algorithm can rely on a larger amount of signal energy before and after the gated portion of the data to reconstruct the time series. NNETFIX successfully reconstructs over two thirds of the time series with $\rho_N=28.3$ or larger for all low-mass and medium-mass exploration sets and over half of the time series for the high-mass sets with the exception of two marginal cases with gate duration $t_d=75$ ms and gate end-time $t_e=90$ ms. The exploration sets with $\rho_N=11.3$ exhibit lower efficiencies, ranging from 31% for the high-mass set with $t_d=75$ ms and $t_e=90$ ms to 66% for the low-mass set with $t_d=130$ ms and

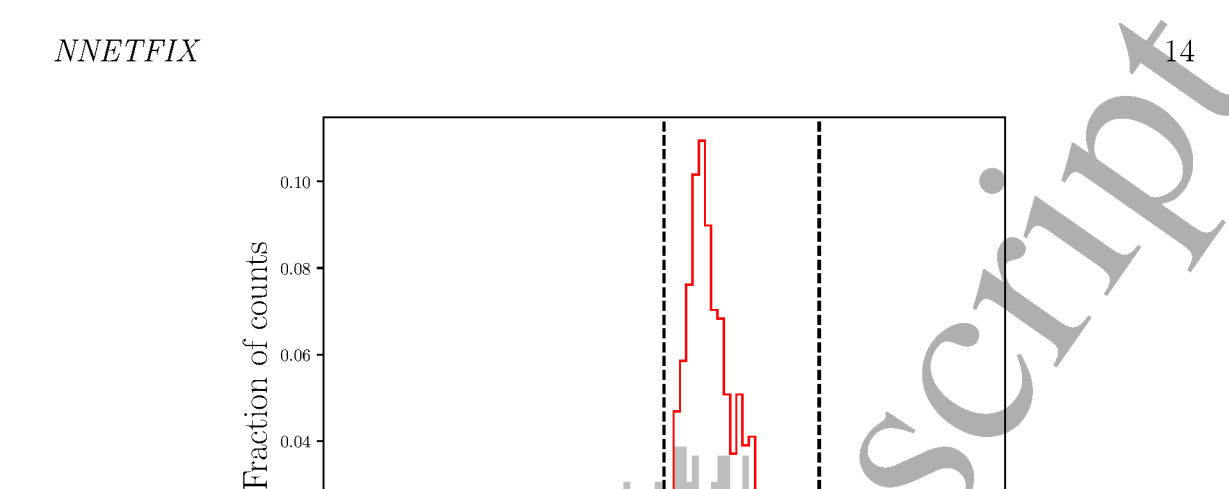


Figure 6. Distribution of FMG for the exploration sets with component masses $(m_1,m_2)=(20,15)~M_{\odot}$, gate duration $t_d=130$ ms, gate end-time $t_e=30$ ms, and $\rho_N = 11.3$ (gray-filled) and $\rho_N = 42.4$ (red). The vertical dashed lines denote FMG= 0 and FMG= 1. The efficiency of the set with $\rho_N=11.3$ is 59%. The efficiency of the set with $\rho_N = 42.3$ is 95%.

FMG

 $t_e = 15 \text{ ms.}$

0.04

0.02

0.00

Figure 7 shows the efficiency for the exploration sets with component masses $(m_1, m_2) = (20, 15) M_{\odot}$ as a function of the single interferometer peak SNR. The percentage of successful reconstructions ranges from $\sim 33\%$ –66% at low peak SNR to $\gtrsim 80\%$ at high peak SNR, with the lowest values $\lesssim 40\%$ occurring for the sets with $t_d \geq 75$ ms and $t_e \geq 30$ ms. Time series with peak SNR above ~ 20 show successful reconstructions in 70% or more of the cases, irrespective of gate duration and end-time.

Changing the gate duration does not seem to have a significant effect on NNETFIX's efficiency, which only varies slightly at fixed network SNR and gate end-time across all exploration sets. Similarly, for fixed gate duration and network SNR, the gate end-time before merger time also has a marginal effect, although NNETFIX tends to produce better reconstructions when the gate is closer to the merger time, especially for long gate durations in the low-mass and medium-mass



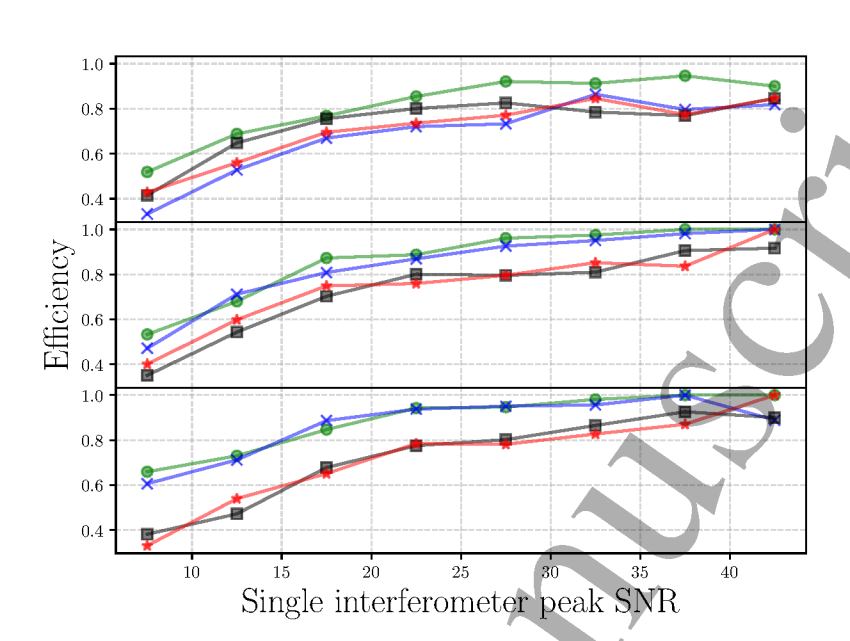


Figure 7. Efficiency as a function of the single interferometer peak SNR for the scenario with component masses $(m_1, m_2) = (20, 15) \ M_{\odot}$. Each line corresponds to a different gate duration and gate end-time combination. The top (middle, bottom) panel shows the efficiency for $t_d = 50$ (75, 130) ms. Green circle (blue cross, black square, red star) markers denote gate end-times $t_e = 15$ (30, 90, 170) ms. The efficiency is calculated for the samples within a bin of width 5 centered on each point.

scenarios.

In conclusion, we find that NNETFIX may successfully reconstruct gated data of durations up to a few hundreds of milliseconds and as close as a few tens of milliseconds before the merger time for a majority of time series with single interferometer peak SNR greater than 20.

4. Performance of sky maps

The NNETFIX reconstructed time series can be used to produce sky maps that are expected to have better sky localization error regions of the astrophysical signal in comparison to sky maps produced from the gated time series. We evaluate this improvement by comparing the overlaps of the sky map derived from the full time series with the sky maps derived from the gated time series and the reconstructed

time series. In the following, we generate the sky maps with a modified version of a pyCBC [43] script, PYCBC_MAKE_SKYMAP, in which the data can be manually gated.

Similar to Ref. [44], we define the overlap of two sky maps (1,2) as

$$O_{1,2} = \frac{4\pi \int p_1(\Omega) p_2(\Omega) d\Omega}{\int p_1(\Omega) d\Omega \int p_2(\Omega) d\Omega},$$
(7)

where $p_1(\Omega)$ and $p_2(\Omega)$ are the sky localization probability densities of the sky maps in units of inverse square radians and the integrals are over the solid angle Ω . The discretized version of Eq. (7) is

$$O_{1,2} = N \sum_{i=1}^{N} P_{1i} P_{2i} , \qquad (8)$$

where P_{1i} and P_{2i} each denote the sky localization probability of the *i*-th pixel of the corresponding sky map, and N is the total number of pixels. Each sky map is normalized such that the sum of the pixel values over the entire map is 1. Equation (8) gives values in the range (0, N). Higher values of $O_{1,2}$ indicate a better overlap between the two maps while lower values denote worse overlaps and/or maps which tend to have less-localized error regions. For example, two overlapping sky maps each with a uniform probability distribution would have $O_{1,2} = 1$, while two sky maps with their entire probability distributions confined to the same single pixel would have $O_{1,2} = N$.

A suitable metric to evaluate the improvement in the sky localization of a signal due to NNETFIX's reconstruction is the overlap log ratio (OLR)

$$OLR = \log_{10} \frac{O_{r,f}}{O_{g,f}}, \tag{9}$$

where $O_{r,f}$ ($O_{g,f}$) denote the overlaps of the sky maps obtained with the reconstructed (gated) time series and the full series. Positive (negative) values of OLR indicate that the sky map from the reconstructed time series has a larger (smaller) overlap with the sky map from the full time series than the latter has with the sky map from the gated time series. Tables 5-7 give the fraction of samples with positive OLR for all exploration sets.

High values of OLR are obtained when the overlap of the reconstructed sky map with the sky map from the full time series is large or when the overlap of the gated sky map with the sky map from the full time series is small. The former typically occurs for reconstructed time series with large values of FMG. The latter may happen when the loss of signal due to the gate is high and even small gains in the single interferometer peak SNR have a significant impact on the sky localization.

An example of the OLR distribution as a function of $O_{g,f}$ is shown in Fig. 8 for the exploration set with $\rho_N = 42.4$, component masses $(m_1, m_2) = (20, 15) \ M_{\odot}$, $t_g = 130$ ms and $t_e = 30$ ms. The median value of OLR is $1.14^{+1.15}_{-1.10}$, where the error is a 1- σ percentile. OLR is positive in 87% of the samples. Median values of OLR for all exploration sets are given in Tables 8-10.

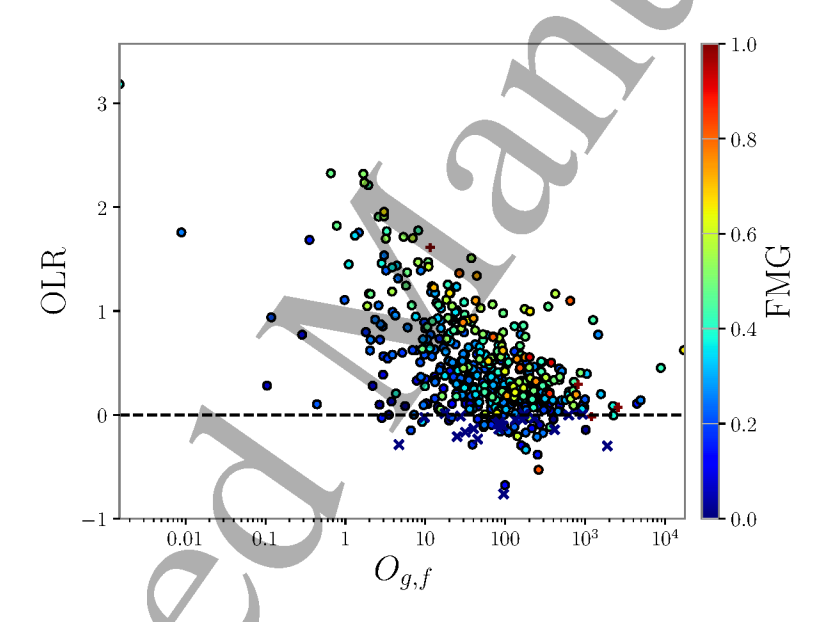


Figure 8. Scatterplot of OLR and $O_{g,f}$ for the 512 samples from the exploration set with $\rho_N = 42.4$, component masses $(m_1, m_2) = (20, 15)~M_{\odot}$, gate end-time $t_e = 30$ ms and gate duration $t_d = 130$ ms. The colored circles denote samples with $0 < \text{FMG} \le 1$, the \times markers denote samples with FMG ≤ 0 and the + markers denote overfitted samples with FMG > 1. 87% of the samples have positive OLR. The median value is OLR= $1.14^{+1.15}_{-1.10}$, where the error is a 1- σ percentile.

Values of OLR across the exploration sets generally increase with network SNR, component masses and gate duration. The network SNR of the signal is the main

factor that determines the value of OLR. Because NNETFIX efficiently reconstructs time series containing signals with large SNRs, when network SNRs are large, the sky maps obtained from the full data are typically more similar to the sky maps from the reconstructed data than to the sky maps from the gated data. We find positive OLR median values for all exploration sets with $\rho_N \geq 28.3$, irrespective of mass, gate duration and end-time. For these sets, the median values of OLR for the high-SNR sets are greater than the corresponding values for the medium-SNR sets by a factor ranging from ~ 1.4 for the high-mass scenario with $t_d = 130$ ms and $t_e = 15$ ms to ~ 5 for the low-mass scenario with $t_d = 75$ ms and $t_e = 170$ ms. The sky maps of reconstructed time series with lower SNR generally show little improvement compared with the sky maps of gated time series. Median values of OLR for the sets with $\rho_N = 11.3$ are typically around zero, irrespective of the mass scenario, gate duration and gate end-time.

The second most important factor that determines OLR are the component masses. Median OLR values typically increase as values of the component masses become larger. For the exploration sets with $\rho_N = 28.3$ (42.4), the median values of OLR for the high-mass exploration sets are greater than the corresponding values for the low-mass exploration sets by a factor ranging from ~ 1.5 (2.3) for $t_d = 130$ ms and $t_e = 90$ ms ($t_d = 130$ ms and $t_e = 15$ ms) to ~ 20.5 (12.6) for $t_d = 50$ ms and $t_e = 15$ ms ($t_d = 50$ ms and $t_e = 30$ ms).

Median values of OLR have a roughly linear dependency on gate duration. For the high-SNR and medium-SNR exploration sets, the median values of OLR for $t_d = 130$ ms are larger than the corresponding values for $t_d = 50$ ms by a factor ranging from ~ 1.6 (medium-mass scenario with $\rho_N = 42.4$ and $t_e = 15$ ms) to ~ 4.7 (high-mass scenario with $\rho_N = 28.3$ and $t_e = 90$ ms). Since longer gate durations correspond to greater signal losses, NNETFIX's reconstruction provides larger SNR gains and OLR values as the gate duration increases.

The portion of a signal close to the merger time has a greater impact on the sky map than the portion of the signal in the early inspiral phase. Therefore, median values of OLR for the medium-SNR and high-SNR exploration sets with $t_e = 15$ ms are typically higher than the corresponding values for the sets with $t_e = 170$ ms by a factor ranging from ~ 1.1 (low-mass scenario with $\rho_N = 28.3$ and $t_d = 90$ ms) to ~ 7.1 (high-mass scenario with $\rho_N = 28.3$ and $t_d = 50$ ms). For shorter signals and larger gate durations, a gate end-time very close to the merger time may lead to large signal losses and removal of the merger portion of the signal in H1, and thus,

make the reconstruction process less efficient. Figure 9 shows OLR as a function of the gate end-time for the high-mass sets with $t_d = 130$ ms and different network SNRs. Figure 10 shows the sky localization error region that is obtained with the NNETFIX reconstructed data for the case of Fig. 1. The value of OLR is ~ 1.7 , corresponding to improving the overlap by a factor of ~ 50 .

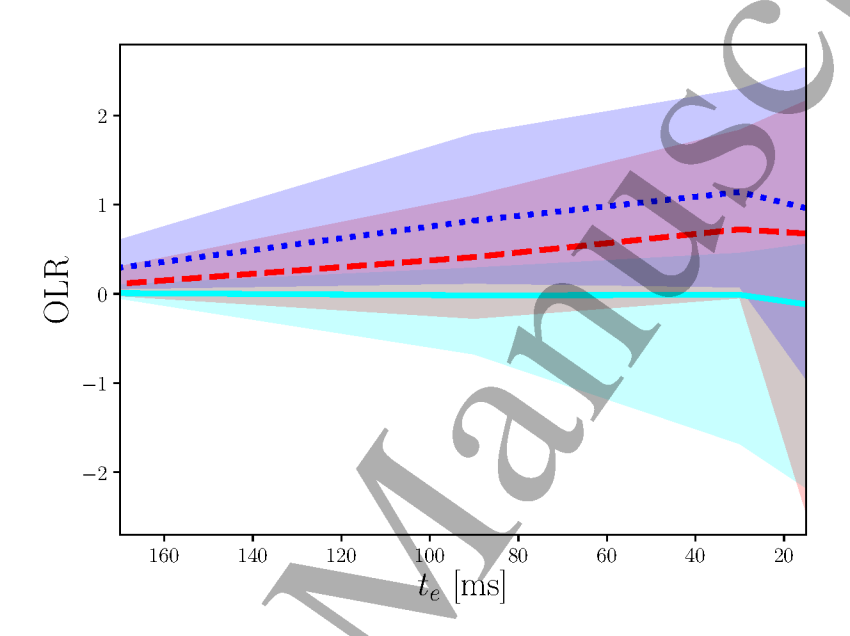


Figure 9. OLR as a function of the gate end-time t_e for the exploration set with component masses $(m_1, m_2) = (35, 29) \ M_{\odot}$, gate duration $t_d = 130$ ms, and different network SNRs $\rho_N = 11.3$ (cyan solid), $\rho_N = 28.3$ (red dashed), and $\rho_N = 42.4$ (blue dashed). The curves denote median values. Shaded areas are 1- σ percentiles.

In summary, for a majority of the cases with gate durations up to a few hundreds of milliseconds and as close as a few tens of milliseconds to the merger time, the sky maps of reconstructed time series with network SNR $\rho_N \geq 28.3$ better overlap with the sky maps of the full time series compared to the sky maps obtained with gated data (in some cases by a factor up to over 1000%). In these cases, it can also be shown that the true direction of the signals typically belong to sky localization error regions for the reconstructed data with smaller probability contour values than the regions obtained with gated data.

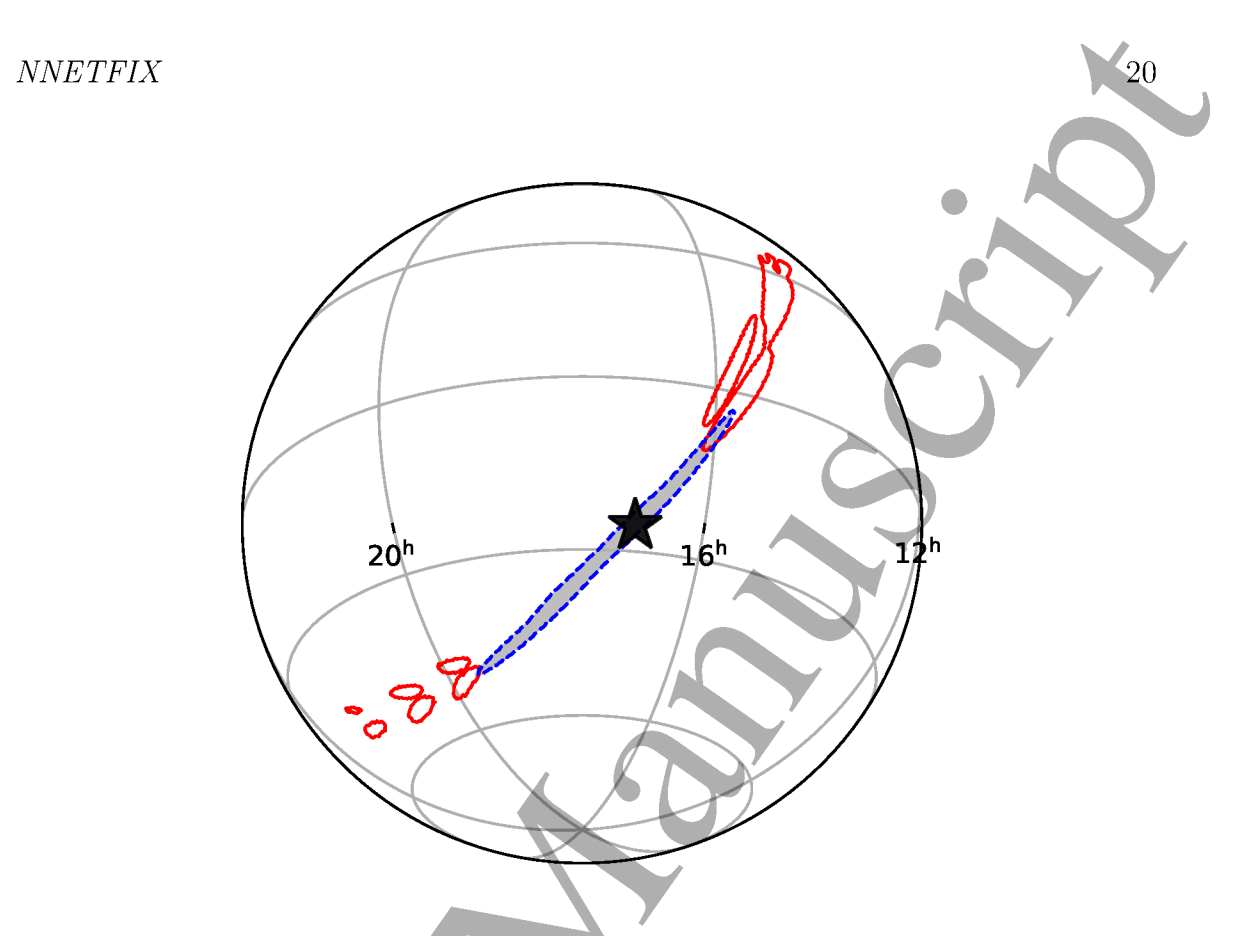


Figure 10. The 90% probability sky localization error regions obtained with the reconstructed (dashed-blue), full (gray area) and gated (solid-red) time series for the case of Fig. 1. The star denotes the injection location.

5. Conclusion

In this paper, we have presented NNETFIX, a new machine learning-based algorithm designed to estimate the portion of a BBH GW signal that may be gated due to the presence of an overlapping glitch. The reconstructed data can be used by other algorithms to produce better sky maps and for parameter estimation. We have tested the accuracy of NNETFIX with different choices of signal parameters and gate settings, and defined several metrics to assess the algorithm's performance. Among these metrics, the most important ones are FMG and OLR.

FMG quantifies the algorithm's efficiency in reconstructing the gated data in the time domain. Positive values of this metric indicate that the full time series

better matches the NNETFIX reconstructed time series than the gated time series. The fraction of samples that show improvement varies from approximately one third to over 95% across the cases that we investigated. Results show that NNETFIX may be able to successfully reconstruct a majority of BBH signals with peak single interferometer SNR greater than 20 and gates with durations up to a few hundreds of milliseconds as close as a few tens of milliseconds before their merger time.

OLR quantifies the algorithm's efficiency in improving the sky map from the gated time series. Positive values of this metric indicate that the sky map from the NNETFIX reconstructed time series has a larger overlap with the sky map from the full time series than the one obtained from the gated data. Sky maps from reconstructed data improve for higher network SNR values as the ANN can use a larger amount of signal energy to estimate the missing portion of the waveform. We find positive OLR median values for all cases that we investigated with network SNR above 28.3. Perhaps surprisingly, NNETFIX seems also to perform better in cases with longer gate durations or shorter signals. In these scenarios, the sky localizations obtained with gated data are considerably degraded. Thus, the improvements in the reconstructed sky maps are more sizeable. Reconstructed sky maps of more massive BBH mergers typically show significant improvements compared to the sky maps obtained with gated data.

In a real case scenario, we envision NNETFIX to be pre-trained on real noise data from the detectors for a sparse set of models, each covering a region of the five-dimensional parameter space spanned by network SNR, component masses, gate duration, and gate end-time before geocentric merger time, as was illustrated in Sec. 2 (but with a finer grid). While the optimal value of the network SNR and the best estimates of the signal component masses are unknown to the observer because of the gating, the gated data and/or the data from the second interferometer may provide a rough estimate of these parameters. The estimated values of these parameters and the known gate parameters can then be used to choose the most appropriate pre-trained model in the NNETFIX bank. Typically, the NNETFIX reconstructed time series will produce a higher single interferometer peak SNR than the gated time series. If that is the case, the known FSG can be used to estimate the optimal single interferometer peak SNR of the (unknown) full time series by fitting the expected roughly linear relation between FRS and FSG for the given TT set.

The overlap of the sky map from the NNETFIX reconstructed data with the sky map that could be obtained with the full data (if it were not contaminated by a

glitch), $O_{r,f}$, can be estimated by looking at the distribution of OLR for the TT set at hand. The exploration sets that we investigated show that there is a well-defined correlation between OLR, FSG and the overlap between the sky maps obtained from the gated data and the NNETFIX reconstructed data, $O_{r,g}$. If this correlation is generally valid, OLR can be estimated from the observed values of the $O_{r,g}$ and FSG using a fit calculated from the TT set used to train the selected NNETFIX model. To expedite this process, the samples in each TT set could be clustered according to the distributions of OLR, the $O_{r,g}$, and FSG. A classifier could then be trained to estimate the optimal SNR and sky localization error region of the full signal.

Once NNETFIX has been trained, the CPU time required to reconstruct the data is of the order of a few seconds for gate durations up to hundreds of milliseconds. This short turnout makes the algorithm suitable to be used in low-latency. Additional machine learning-based algorithms could also be implemented to further speed up the sky localization portion of the process. For example, the method described in Ref. [25] may produce sky localizations with an execution time on the order of 0.01 seconds, making this method an interesting option for generating low-latency sky maps. NNETFIX could also be applied to GW signals other than BBH mergers, such as BNS or NSBH mergers. Therefore, it could be beneficial for rapid follow-up of glitch-contaminated, potentially EM-bright candidate detections. In future work, we intend to test NNETFIX on real BBH detections and explore the algorithm's application to BNS signals as well as detector network configurations with more than two detectors. Improving the sky localizations of potentially EM-bright signals could increase the chances of coincident EM and GW observations and lead to a better understanding of the physical properties of their sources.

Acknowledgements

K.M., R.Q.J., and M.C. are supported by the U.S. National Science Foundation grants PHY-1921006 and PHY-2011334. The authors would like to thank their LIGO Scientific Collaboration and Virgo Collaboration colleagues for their help and useful comments, in particular Tito Dal Canton. The authors are grateful for computational resources provided by the LIGO Laboratory and supported by the U.S. National Science Foundation Grants PHY-0757058 and PHY-0823459, as well as resources from the Gravitational Wave Open Science Center, a service of the LIGO Laboratory, the LIGO Scientific Collaboration and the Virgo Collaboration. Part of this research

has made use of data, software and web tools obtained from the Gravitational Wave Open Science Center and openly available at https://www.gw-openscience.org. LIGO was constructed and is operated by the California Institute of Technology and Massachusetts Institute of Technology with funding from the U.S. National Science Foundation under grant PHY-0757058. Virgo is funded by the French Centre National de la Recherche Scientifique (CNRS), the Italian Istituto Nazionale di Fisica Nucleare (INFN) and the Dutch Nikhef, with contributions by Polish and Hungarian institutes. This manuscript has been assigned LIGO Document Control Center number LIGO-P2000497.

References

- [1] Abbott B P et al. (Virgo, LIGO Scientific) 2016 Phys. Rev. Lett. 116 061102 (Preprint 1602.03837)
- [2] Aasi J et al. (LIGO Scientific) 2015 Class. Quant. Grav. 32 074001 (Preprint 1411.4547) URL http://stacks.iop.org/0264-9381/32/i=7/a=074001
- [3] Acernese F et al. (VIRGO) 2015 Class. Quant. Grav. 32 024001 (Preprint 1408.3978) URL http://stacks.iop.org/0264-9381/32/i=2/a=024001
- [4] Abbott B P et al. (LIGO Scientific Collaboration and Virgo Collaboration) 2019 Phys. Rev. X 9(3) 031040 URL https://link.aps.org/doi/10.1103/PhysRevX.9.031040
- [5] Abbott R et al. (LIGO Scientific, Virgo) 2020 (Preprint 2010.14527)
- [6] Abbott R et al. (LIGO Scientific, Virgo) 2020 Phys. Rev. D 102 043015 (Preprint 2004.08342)
- [7] Abbott R et al. (LIGO Scientific Collaboration and Virgo Collaboration) 2020 Phys. Rev. Lett. 125(10) 101102 URL https://link.aps.org/doi/10.1103/PhysRevLett.125.101102
- [8] Abbott R et al. 2020 The Astrophysical Journal 900 L13 URL https://doi.org/10.3847% 2F2041-8213%2Faba493
- [9] Abbott R et al. (LIGO Scientific, Virgo) 2020 Astrophys. J. 896 L44 (Preprint 2006.12611)
- [10] Abbott B P et al. (LIGO Scientific Collaboration and Virgo Collaboration) 2017 Phys. Rev. Lett. 119(16) 161101 URL https://link.aps.org/doi/10.1103/PhysRevLett.119. 161101
- [11] Abbott B P et al. (GROND, SALT Group, OzGrav, DFN, INTEGRAL, Virgo, Insight-Hxmt, MAXI Team, Fermi-LAT, J-GEM, RATIR, IceCube, CAASTRO, LWA, ePESSTO, GRAWITA, RIMAS, SKA South Africa/MeerKAT, H.E.S.S., 1M2H Team, IKI-GW Follow-up, Fermi GBM, Pi of Sky, DWF (Deeper Wider Faster Program), Dark Energy Survey, MASTER, AstroSat Cadmium Zinc Telluride Imager Team, Swift, Pierre Auger, ASKAP, VINROUGE, JAGWAR, Chandra Team at McGill University, TTU-NRAO, GROWTH, AGILE Team, MWA, ATCA, AST3, TOROS, Pan-STARRS, NuSTAR, ATLAS Telescopes, BOOTES, CaltechNRAO, LIGO Scientific, High Time Resolution Universe Survey, Nordic Optical Telescope, Las Cumbres Observatory Group, TZAC Consortium, LOFAR, IPN,

DLT40, Texas Tech University, HAWC, ANTARES, KU, Dark Energy Camera GW-EM, CALET, Euro VLBI Team, ALMA) 2017 Astrophys. J. 848 L 12 (Preprint 1710.05833)

- [12] Abbott B P et al. (Virgo, Fermi-GBM, INTEGRAL, LIGO Scientific) 2017 Astrophys. J. 848 L13 (Preprint 1710.05834)
- [13] Abbott B et al. (LIGO Scientific, Virgo) 2020 Astrophys. J. Lett. 892 L3 (Preprint 2001) 01761)
- [14] Driggers J et al. (LIGO Scientific) 2019 Phys. Rev. D 99 042001 (Preprint 1806, 00532)
- [15] Zevin M, Coughlin S, Bahaadini S, Besler E, Rohani N, Allen S, Cabero M, Crowston K, Katsaggelos A K, Larson S L, Lee T K, Lintott C, Littenberg T B, Lundgren A, Østerlund C, Smith J R, Trouille L and Kalogera V 2017 Classical and Quantum Gravity 34 064003 URL https://doi.org/10.1088/1361-6382/aa5cea
- [16] Usman S A et al. 2016 Class. Quant. Grav. 33 215004 (Preprint 1508.02357)
- [17] Pankow C et al. 2018 Phys. Rev. D 98(8) 084016 URL https://link.aps.org/doi/10.1103/ PhysRevD.98.084016
- [18] Cornish N J and Littenberg T B 2015 Classical and Quantum Gravity 32(13) 135012 URL https://doi.org/10.1088/0264-9381/32/13/135012
- [19] Chatziioannou K, Cornish N, Wijngaarden M and Littenberg T B 2021 (Preprint 2101.01200)
- [20] Cornish N J 2021 Rapid and Robust Parameter Inference for Binary Mergers (*Preprint* 2101.01188)
- [21] Cuoco E, Powell J, Cavaglià M, Ackley K, Bejger M, Chatterjee C, Coughlin M, Coughlin S, Easter P, Essick R, Gabbard H, Gebhard T, Ghosh S, Haegel L, Iess A, Keitel D, Márka Z, Márka S, Morawski F, Nguyen T, Ormiston R, Pürrer M, Razzano M, Staats K, Vajente G and Williams D 2020 Machine Learning: Science and Technology 2 011002 URL https://doi.org/10.1088/2632-2153/abb93a
- [22] Torres-Forné A, Cuoco E, Marquina A, Font J A and Ibáñez J M 2018 Phys. Rev. D 98(8) 084013 URL https://link.aps.org/doi/10.1103/PhysRevD.98.084013
- [23] Ormiston R, Nguyen T, Coughlin M, Adhikari R X and Katsavounidis E 2020 Phys. Rev. Research 2(3) 033066 URL https://link.aps.org/doi/10.1103/PhysRevResearch.2.033066
- [24] Wei W and Huerta E 2020 Physics Letters B 800 135081 ISSN 0370-2693 URL http://www.sciencedirect.com/science/article/pii/S0370269319308032
- [25] Chatterjee C, Wen L, Vinsen K, Kovalam M and Datta A 2019 Phys. Rev. D 100(10) 103025 URL https://link.aps.org/doi/10.1103/PhysRevD.100.103025
- [26] Singer L P and Price L R 2016 Phys. Rev. D 93(2) 024013 URL https://link.aps.org/doi/ 10.1103/PhysRevD.93.024013
- [27] LIGO Scientific Collaboration 2018 LIGO Algorithm Library LALSuite free software (GPL)
- [28] Ashton G, Hübner M, Lasky P D, Talbot C, Ackley K, Biscoveanu S, Chu Q, Divakarla A, Easter P J, Goncharov B, Vivanco F H, Harms J, Lower M E, Meadors G D, Melchor D, Payne E, Pitkin M D, Powell J, Sarin N, Smith R J E and Thrane E 2019 The Astrophysical Journal Supplement Series 241 27 URL https://doi.org/10.3847/1538-4365/ab06fc
- [29] Robinet F-2018 Omicron: an algorithm to detect and characterize transient events in gravitational-wave detectors Tech. rep. https://tds.ego-gw.it/?content=3&r=14693

[30] Essick R 2017 Detectability of dynamical tidal effects and the detection of gravitational-wave transients with LIGO Ph.D. thesis Massachusetts Institue of Technology http://hdl.handle.net/1721.1/115024

- [31] Essick R, Godwin P, Blackburn L and Katsavounidis E 2020 (Preprint 2005.12761)
- [32] Pedregosa F, Varoquaux G, Gramfort A, Michel V, Thirion B, Grisel O, Blondel M, Prettenhofer P, Weiss R, Dubourg V, Vanderplas J, Passos A, Cournapeau D, Brucher M, Perrot M and Duchesnay E 2011 Journal of Machine Learning Research 12 2825–2830
- [33] Rosenblatt F 1961 Principles of neurodynamics. perceptrons and the theory of brain mechanisms Tech. rep. Cornell Aeronautical Lab Inc Buffalo NY
- [34] Hahnloser R H R, Sarpeshkar R, Mahowald M A, Douglas R J and Seung H S 2000 Nature 405 947–51 URL https://doi.org/10.1038/35016072
- [35] Nair V and Hinton G E 2010 Rectified linear units improve restricted boltzmann machines Proceedings of the 27th International Conference on International Conference on Machine Learning ICML'10 (Madison, WI, USA: Omnipress) p 807–814 ISBN 9781605589077
- [36] Kingma D and Ba J 2014 International Conference on Learning Representations
- [37] Khan S, Husa S, Hannam M, Ohme F, Pürrer M, Forteza X J and Bohé A 2016 Phys. Rev. D 93(4) 044007 URL https://link.aps.org/doi/10.1103/PhysRevD.93.044007
- [38] Cokelaer T 2007 Phys. Rev. D 76 102004 (Preprint 0706, 4437)
- [39] Harry I W, Allen B and Sathyaprakash B 2009 Phys. Rev. D 80 104014 (Preprint 0908.2090)
- [40] Van Den Broeck C, Brown D A, Cokelaer T, Harry I, Jones G, Sathyaprakash B, Tagoshi H and Takahashi H 2009 Phys. Rev. D 80 024009 (Preprint 0904.1715)
- [41] Manca G M and Vallisneri M 2010 Phys. Rev. D 81 024004 (Preprint 0909.0563)
- [42] Chatterji S, Blackburn L, Martin G and Katsavounidis E 2004 Class. Quant. Grav. 21 S1809–S1818 (Preprint gr-qc/0412119)
- [43] Nitz A, Harry I, Brown D, Biwer C M, Willis J, Canton T D, Capano C, Pekowsky L, Dent T, Williamson A R, Davies G S, De S, Cabero M, Machenschalk B, Kumar P, Reyes S, Macleod D, Pannarale F, dfinstad, Massinger T, Tápai M, Singer L, Khan S, Fairhurst S, Kumar S, Nielsen A, shasvath, Dorrington I, Lenon A and Gabbard H 2020 gwastro/pycbc: Pycbc release 1.16.4 URL https://doi.org/10.5281/zenodo.3904502
- [44] Ashton G, Burns E, Canton T D, Dent T, Eggenstein H B, Nielsen A B, Prix R, Was M and Zhu S J 2018 The Astrophysical Journal 860 6 URL https://doi.org/10.3847%2F1538-4357%2Faabfd2

| Network SNR | SNA | دم | 11.3 | | | 28.3 | | | 42.4 | |
|------------------------|-----|--|-------------------------|-------------------------|-------------------------|--|-------------------------|-------------------------|-------------------------|----------------|
| $t_d \; [\mathrm{ms}]$ | [S] | 50 | 75 | 130 | 50 | 75 | 130 | 50 | 75 | 130 |
| | 15 | 15 0.33/0.54/0.14 0.34/0.55/ | 0.34/ 0.55 /0.11 | 0.31/0.66/0.04 | 0.21/0.76/0.03 | $ \sqrt{0.11} \ \ 0.31 / \ 0.66 / \ 0.04 \ \ 0.21 / \ 0.76 / \ 0.03 \ \ 0.13 / \ 0.88 / \ 0.00 \ \ 0.10 / \ 0.84 / \ 0.00 \ \ 0.10 / \ 0.88 / \ 0.02 \ \ 0.07 / \ 0.93 / \ 0.01 \ \ 0.06 / \ 0.94 / \ 0.00 $ | 0.16/0.84/0.00 | 0.10/0.88/0.02 | 0.07/0.93/0.01 | 0.06/0.94/0.00 |
| $t_e [\mathrm{ms}]$ | 30 | $30 \boxed{0.30/0.46/0.24 6.31/0.46/0.23 0.29/\textbf{0.63}/0.08 0.15/\textbf{0.78}/0.07 0.16/\textbf{0.80}/0.04 0.16/\textbf{0.84}/0.01 0.06/\textbf{0.88}/0.06 0.04/\textbf{0.93}/0.04 0.06/\textbf{0.94}/0.01 0.06/\textbf{0.88}/0.06 0.04/\textbf{0.93}/0.04 0.06/\textbf{0.94}/0.01 0.06/\textbf{0.88}/0.06 0.04/\textbf{0.93}/0.04 0.06/\textbf{0.94}/0.01 0.06/\textbf{0.98}/0.06 0.04/\textbf{0.93}/0.04 0.06/\textbf{0.94}/0.01 0.06/\textbf{0.98}/0.04 0.0$ | 0.31/0.46/0.23 | 0.29/ 0.63 /0.08 | 0.15/0.78/0.07 | 0.16/ 0.80 /0.04 | 0.16/0.84/0.01 | 0.06/ 0.88 /0.06 | 0.04/ 0.93 /0.04 | 0.06/0.94/0.01 |
| , | 90 | 90 $\parallel 0.28/0.39/0.33 \mid 0.32/0.36$ | | 0.31/0.52/0.17 | 0.10/0.69/0.21 | $0.32 0.31/0.52/0.17 0.10/0.69/0.21 0.15/0.71/0.13 0.14/0.82/0.05 0.03/0.80/0.17 0.07/0.84/0.09 0.07/0.92/0.01 \\ 0.07/0.92/0.01 0.07/0.92/0.01 \\ 0.07/0.92/0.01 0.07/0.92/0.01 \\ 0.07/0.92/0.01$ | 0.14/ 0.82 /0.05 | 0.03/0.80/0.17 | 0.07/ 0.84 /0.09 | 0.07/0.92/0.01 |
| | 170 | $170 \parallel 0.28/0.40/0.33 \mid 0.31/0.40/$ | 0.31/0.40/0.29 | 0.34/0.38/0.27 | 0.09/ 0.68 /0.23 | 9.34/0.38/0.27 0.09/ 0.68 /0.23 0.15/ 0.71 /0.14 0.21/ 0.67 /0.12 0.02/ 0.84 /0.14 0.05/ 0.83 /0.13 0.11/ 0.83 /0.06 0.0000000000000000000000000000000 | 0.21/0.67/0.12 | 0.02/ 0.84 /0.14 | 0.05/ 0.83 /0.13 | 0.11/0.83/0.06 |

Table 2. Fraction of samples with FMG ≤ 0 , $0 < \text{FMG} \leq 1$ and FMG > 1 for the exploration sets with component masses $(m, m_0) = (19, 10)M_{\odot}$. Boldform with $(m, m_0) = (19, 10)M_{\odot}$. Boldform

| | | $(m_1, m_2) = (12, 10)N$ | $(12, 10) M_{\odot}$. | Boldiace entri | es denote sets | where the ire | action of samp | I_{\odot} . Boldiace entries denote sets where the fraction of samples with $0 < FMG \le 1$ is larger than 50% . | MG≤1 is la | rger than 50% |
|------------------------|-----|--|------------------------|-------------------------|-------------------------|-------------------------|-------------------------------|---|-------------------------|-------------------------|
| Network SNR | SNR | نہ | 11.3 | | | 28.3 | | | 42.4 | |
| $t_d \; [\mathrm{ms}]$ | [sı | 50 | 75 | 130 | 50 | 75 | 130 | 50 | 75 | 130 |
| | 15 | $15 \left\ 0.28/0.52/0.19 0.31/0.55/0.15 0.29/0.64/0.06 0.12/0.78/0.10 0.14/0.83/0.03 0.13/0.87/0.01 0.04/0.89/0.06 0.04/0.94/0.02 0.05/0.95/0.00 \right\}$ | 0.31/0.55/0.15 | 0.29/ 0.64 /0.06 | 0.12/0.78/0.10 | 0.14/0.83/0.03 | 0.13/0.87/0.01 | 0.04/0.89/0.06 | 0.04/0.94/0.02 | 0.05/0.95/0.00 |
| $t_e \; [\mathrm{ms}]$ | 30 | $t_{e} \; [\mathrm{ms}] 30 \; \left\ \; 0.29/0.34/0.37 \; \; 0.29/0.49/0.22 \; \; 0.31/0.59/0.10 \; \; 0.11/0.68/0.21 \; \; 0.40/0.88/0.08 \; \; 0.11/0.88/0.01 \; \; 0.04/0.75/0.21 \; \; 0.05/0.91/0.04 \; \; 0.04/0.75/0.01 \; \; 0.05/0.91/0.04 \; \; 0.04/0.75/0.01 \; \; 0.05/0.91/0.04 \; \; 0.04/0.75/0.01 \; \; 0.05/0.91/0.04 \; \; 0.04/0.95/0.01 \; \; 0.04/0.75/0.01 \; $ | 0.29/0.49/0.22 | 0.31/0.59/0.10 | 0.11/ 0.68 /0.21 | 0.10/0.82/0.08 | 0.11/ 0.88 /0.01 | 0.04/ 0.75 /0.21 | 0.05/0.91/0.04 | 0.04/ 0.95 /0.01 |
| | 90 | $90 \parallel 0.24/0.42/0.34 0.30/0.38/0.32 0.29/0.39/0.32 0.04/0.76/0.20 0.08/0.72/0.20 0.17/0.69/0.15 0.02/0.79/0.20 0.03/0.79/0.19 0.10/0.80/0.10 0.03/0.79/0.20 0.03/0.79/0.19 0.10/0.80/0.10 0.03/0.79/0.10 0.03/0$ | 0.30/0.38/0.32 | 0.29/0.39/0.32 | 0.04/0.76/0.20 | 0.08/0.72/0.20 | 0.17/0.69/0.15 | 0.02/ 0.79 /0.20 | 0.03/0.79/0.19 | 0.10/ 0.80 /0.10 |
| | 170 | $170 \parallel 0.20/0.42/0.37 0.26/0.42/0.32 0.31/0.32/0.36 0.04/0.69/0.27 0.04/0.72/0.23 0.11/0.69/0.19 0.01/0.78/0.21 0.01/0.80/0.19 0.06/0.79/0.15$ | 0.26/0.42/0.32 | 0.31/0.32/0.36 | 0.04/ 0.69 /0.27 | 0.04/ 0.72 /0.23 | $0.11/\boldsymbol{0.69}/0.19$ | 0.01/ 0.78 /0.21 | 0.01/ 0.80 /0.19 | 0.06/ 0.79 /0.15 |

Table 3. Fraction of samples with FMG ≤ 0 , $0 < \text{FMG} \leq 1$ and FMG > 1 for the exploration sets with component masses $(m_1, m_2) = (20, 15)M_{\odot}$. Boldface entries denote sets where the fraction of samples with $0 < \text{FMG} \le 1$ is larger than 50%.

| Network SNR | dR. | 11.3 | | | 28.3 | 7 | | 42.4 | |
|---------------------|--|------------------|----------------|-------------------------|---|-------------------------|----------------|-------------------------|-------------------------|
| $t_d [\mathrm{ms}]$ | 50 | 75 | 130 | 50 | 75 | 130 | 50 | 75 | 130 |
| 11 | 15 0.19/ 0.50 /0.31 0.27/ 0.53 / | 1 0.27/0.53/0.20 | 0.25/0.44/0.31 | 0.04/0.76/0.20 | $0.20 \ \ 0.25/0.44/0.31 \ \ 0.04/0.76/0.20 \ \ 0.05/0.84/0.11 \ \ 0.07/0.76/0.17 \ \ 0.02/0.80/0.19 \ \ 0.02/0.90/0.08 \ \ 0.02/0.81/0.17 $ | 0.07/0.76/0.17 | 0.02/0.80/0.19 | 0.02/0.90/0.08 | 0.02/0.81/0.17 |
|] 3(| $t_{e} \; [\mathrm{ms}] 30 \; \left\ \; 0.21/0.35/0.45 \; \; 0.24/0.34/0.42 \; \; 0.24/0.44/0.32 \; \; 0.03/0.60/0.37 \; \; 0.03/0.56/0.41 \; \; 0.05/0.76/0.41 \; \; 0.05/0.76/0.37 \; \; 0.03/0.66/0.37 \; \; 0.03/0.66/0.31 \; \; 0.02/0.86/0.12 \; \; 0.03/0.66/0.31 \; \; 0$ | 0.24/0.34/0.42 | 0.24/0.44/0.32 | 0.03/0.60/0.37 | 0.03/ 0.56 /0.41 | 0.05/0.76/0.19 | 0.01/0.62/0.37 | 0.03/0.66/0.31 | 0.02/ 0.86 /0.12 |
| 96 | 90 0.17/0.47/0.36 0.12/0.31/0 | 0.12/0.31/0.57 | 0.21/0.32/0.47 | 0.01/ 0.75 /0.24 | 0.57 0.21/0.32/0.47 0.01/ 0.75 /0.24 0.02/0.42/0.57 0.04/ 0.51 /0.46 0.00/ 0.79 /0.21 0.00/0.38/0.62 0.01/ 0.59 /0.40 0.00/0.38/0.62 0.01/0.28/0.62 0. | 0.04/ 0.51 /0.46 | 0.00/0.79/0.21 | 0.00/0.38/0.62 | 0.01/ 0.59 /0.40 |
| 17 | $170 \parallel 0.14/0.42/0.44 0.15/0.40/0.45 0.22/0.45/0.33 0.01/0.63/0.36 0.01/0.64/0.35 0.05/0.75/0.20 0.01/0.67/0.32 0.00/0.65/0.35 0.01/0.88/0.11$ | 0.15/0.40/0.45 | 0.22/0.45/0.33 | 0.01/ 0.63 /0.36 | 0.01/0.64/0.35 | 0.05/0.75/0.20 | 0.01/0.67/0.32 | 0.00/ 0.65 /0.35 | 0.01/0.88/0.11 |

Table 4. Fraction of samples with FMG ≤ 0 , $0 < \text{FMG} \leq 1$ and FMG > 1 for the exploration sets with component masses $(m_1,m_2)=(35,29)M_{\odot}$. Boldface entries denote sets where the fraction of samples with $0<{
m FMG}\le 1$ is larger than 50%

| Networl | k SNR | | 11.3 | | | 28.3 | | | 42.4 | |
|---------------------|-------|------|------|------|------|------|------|------|------|------|
| t_d [r | ns] | 50 | 75 | 130 | 50 | 75 | 130 | 50 | 75 | 130 |
| | 15 | 0.52 | 0.53 | 0.56 | 0.62 | 0.71 | 0.74 | 0.76 | 0.83 | 0.87 |
| $t_e [\mathrm{ms}]$ | 30 | 0.56 | 0.53 | 0.52 | 0.68 | 0.73 | 0.76 | 0.81 | 0.85 | 0.91 |
| | 90 | 0.55 | 0.51 | 0.53 | 0.69 | 0.65 | 0.74 | 0.78 | 0.79 | 0.86 |
| | 170 | 0.61 | 0.58 | 0.51 | 0.72 | 0.64 | 0.65 | 0.79 | 0.77 | 0.76 |

Table 5. Fraction of samples with positive OLR for the exploration sets with component masses $(m_1, m_2) = (12, 10) M_{\odot}$.

| Network | SNR | | 11.3 | | | 28.3 | | Y | 42.4 | |
|------------|-----|------|------|------|------|------|------|----------|------|------|
| t_d [n | ns] | 50 | 75 | 130 | 50 | 75 | 130 | 50 | 75 | 130 |
| | 15 | 0.51 | 0.49 | 0.55 | 0.68 | 0.74 | 0.79 | 0.84 | 0.85 | 0.84 |
| t_e [ms] | 30 | 0.46 | 0.48 | 0.51 | 0.69 | 0.76 | 0.80 | 0.85 | 0.88 | 0.88 |
| | 90 | 0.61 | 0.50 | 0.47 | 0.74 | 0.75 | 0.65 | 0.86 | 0.85 | 0.79 |
| | 170 | 0.62 | 0.56 | 0.47 | 0.77 | 0.78 | 0.67 | 0.84 | 0.87 | 0.82 |

Table 6. Fraction of samples with positive OLR for the exploration sets with component masses $(m_1, m_2) = (20, 15) M_{\odot}$. Entries in italic denote sets where the fraction of samples is smaller than 0.5.

| Network | SNR | | 11.3 | | | 28.3 | | | 42.4 | |
|------------|-----|------|------|------|------|------|------|------|------|------|
| t_d [m | s] | 50 | 75 | 130 | 50 | 75 | 130 | 50 | 75 | 130 |
| | 15 | 0.57 | 0.53 | 0.43 | 0.77 | 0.79 | 0.69 | 0.85 | 0.83 | 0.73 |
| t_e [ms] | 30 | 0.51 | 0.45 | 0.49 | 0.81 | 0.81 | 0.82 | 0.91 | 0.87 | 0.87 |
| | 90 | 0.65 | 0.63 | 0.46 | 0.84 | 0.80 | 0.75 | 0.93 | 0.89 | 0.87 |
| | 170 | 0.65 | 0.64 | 0.57 | 0.79 | 0.84 | 0.80 | 0.88 | 0.91 | 0.91 |

Table 7. Fraction of samples with positive OLR for the exploration sets with component masses $(m_1, m_2) = (35, 29)M_{\odot}$. Entries in italic denote sets where the fraction of samples is smaller than 0.5.

| Network | s SNR | | 11.3 | | | 28.3 | | | 42.4 | |
|------------|-------|--------|--------|--------|--------|--------|-------|-------|-------|-------|
| t_d [n | ns] | 50 | 75 | 130 | 50 | 75 | 130 | 50 | 75 | 130 |
| | 15 | 0.0012 | 0.0064 | 0.0096 | 0.016 | 0.031 | 0.056 | 0.051 | 0.086 | 0.14 |
| t_e [ms] | 30 | 0.0044 | 0.0059 | 0.0022 | 0.015 | 0.028 | 0.044 | 0.044 | 0.073 | 0.14 |
| | 90 | 0.0032 | 0.0005 | 0.0021 | 0.0091 | 0.011 | 0.034 | 0.026 | 0.04 | 0.10 |
| | 170 | 0.0026 | 0.0037 | 0.0007 | 0.0076 | 0.0063 | 0.018 | 0.018 | 0.032 | 0.060 |

Table 8. Median values of OLR for the exploration sets with component masses $(m_1, m_2) = (12, 10) M_{\odot}$.

| Network | s SNR | , | 11.3 | | | 28.3 | | | 42.4 | |
|------------|-------|---------|---------|---------|-------|-------|-------|-------|-------|------|
| t_d [n | ns] | 50 | 75 | 130 | 50 | 75 | 130 | 50 | 75 | 130 |
| | 15 | 0.0023 | -0.0007 | 0.016 | 0.054 | 0.087 | 0.17 | 0.16 | 0.24 | 0.32 |
| t_e [ms] | 30 | -0.0050 | -0.0029 | 0.0039 | 0.044 | 0.079 | 0.15 | 0.13 | 0.22 | 0.31 |
| | 90 | 0.0049 | 0.0002 | -0.0051 | 0.025 | 0.046 | 0.050 | 0.074 | 0.13 | 0.25 |
| | 170 | 0.0047 | 0.0051 | -0.0044 | 0.023 | 0.037 | 0.045 | 0.046 | 0.098 | 0.17 |

Table 9. Median values of OLR for the exploration sets with component masses $(m_1, m_2) = (20, 15) M_{\odot}$. Italic entries denote sets with negative values.

| Networ | k SNR | 7 | 11.3 | | | 28.3 | | | 42.4 | |
|------------|-------|--------|--------|---------|-------|-------|------|------|------|------|
| t_d [1 | ms] | 50 | 75 | 130 | 50 | 75 | 130 | 50 | 75 | 130 |
| | 15 | 0.023 | 0.0098 | -0.1400 | 0.33 | 0.45 | 0.68 | 0.62 | 0.82 | 0.96 |
| t_e [ms] | 30 | 0.0032 | -0.043 | -0.0099 | 0.25 | 0.42 | 0.72 | 0.56 | 0.83 | 1.1 |
| | 90 | 0.013 | 0.024 | -0.015 | 0.088 | 0.21 | 0.41 | 0.24 | 0.48 | 0.82 |
| <u>U</u> | 170 | 0.012 | 0.016 | 0.0085 | 0.046 | 0.081 | 0.11 | 0.12 | 0.22 | 0.29 |

Table 10. Median values of OLR for the exploration sets with component masses $(m_1, m_2) = (35, 29) M_{\odot}$. Italic entries denote sets with negative values.